

1 **Controls on earthflow formation in the Teanaway River basin, central** 2 **Washington State, USA**

3 Sarah A. Schanz¹, A. Peyton Colee¹

4 ¹Geology Department, Colorado College, Colorado Springs, 80903, USA

5 *Correspondence to:* Sarah A. Schanz (sschanz@coloradocollege.edu)

6 **Abstract.** Earthflows create landscape heterogeneity, increase local erosion rates, and heighten sediment loads in streams.
7 These slow moving and fine-grained mass movements make up much of the Holocene erosion in the Teanaway River basin,
8 central Cascade Range, Washington State, yet controls on earthflow activity and the resulting topographic impacts are
9 unquantified. We mapped earthflows based on morphologic characteristics and relatively dated earthflow activity using a flow
10 directional surface roughness metric called MADstd. The relative MADstd activity is supported by six radiocarbon ages, three
11 lake sedimentation ages, and 16 cross-cutting relationships, indicating that MADstd is a useful tool to identify and relatively
12 date earthflow activity, especially in heavily vegetated regions. Nearly all of the mapped earthflows are in the Teanaway and
13 lower Roslyn formations, which compose just 32.7% of the study area. Earthflow aspect follows bedding planes in these units,
14 demonstrating a strong lithologic control on earthflow location. Based on absolute ages and MADstd distributions, a quarter
15 of the earthflows in the Teanaway Basin were active in the last few hundred years; the timing coincides with deforestation and
16 increased land use in the Teanaway. Major tributaries initiate in earthflows and valley width is altered by earthflows that create
17 wide valleys upstream and narrow constrictions within the earthflow zone. Although direct sediment delivery from earthflows
18 brings fine sediment to the channel, stream power is sufficient to readily transport fines downstream. Based on our findings,
19 over the Holocene—and particularly in the last few hundred years—lithologic-controlled earthflow erosion in the Teanaway
20 basin has altered valley bottom connectivity and increased delivery of fine sediments to tributary channels.

21 **1 Introduction**

22 Mass movement, including earthflows, transports debris from hillslopes to valley bottoms and can be crucial in creating and
23 maintaining landscape heterogeneity and habitat (Beeson et al., 2018; May et al., 2013). Large wood (LW) transported by
24 mass wasting into the channel results in channel roughness, altered flow hydraulics and sediment transport pathways (Abbe
25 and Montgomery, 1996), and habitat complexity (Burnett et al., 2007). Deep-seated landslides affect valley widths by creating
26 anomalously wide valleys upstream and narrower valleys downstream compared to non-landslide terrain; despite variation in
27 valley width, connectivity between these channels in landslide-prone topography is often higher than in non-landslide prone
28 topography (Beeson et al., 2018; May et al., 2013). In addition to large-scale morphologic changes, landslides can also impact
29 stream health. Landslide-transported silt clogs the pores between stream cobbles and limits oxygen flow to redds (NFTWA,

30 1996), and landslides in narrow tributaries may dam the stream and temporarily kill off a small population (Waples et al.,
31 2008). In landslide-dominated landscapes, understanding the history of landsliding is crucial to reconstructing the development
32 of valley bottom topography.

33

34 In particular, earthflows can have a long-lasting effect on topography, sediment supply, and habitat. Earthflows are fine-grained
35 soil mass movements that move meters or less per year and persist for decades to centuries (Hungr et al., 2014). They tend to
36 occur in clay-bearing rocks or weathered volcanic rocks with translational movement, and are commonly reactivated in
37 response to increased precipitation or other disturbances that decrease shear resistance (Baum et al., 2003). Earthflow
38 movement is correlated to climate and regolith production; over long timescales (10^1 - 10^4 years), earthflow movement is limited
39 by the pace of regolith production as transport typically outpaces weathering rates (Mackey and Roering, 2011). At the annual
40 to decadal scale, precipitation variability is correlated with earthflow speed, in which earthflows are observed to speed up—
41 following a lag of several weeks—after seasonal and annual precipitation increases (Coe, 2012; Handwerger et al., 2013).
42 Droughts may prime earthflows by creating deep desiccation cracks that act as water conduits during ensuing wet conditions
43 (McSaveney and Griffiths, 1987). Although long term droughts cause deceleration of deep (>15 m) earthflows, shallow (<15
44 m deep) earthflows exhibit variable response, as they may be more sensitive to individual storms and short-term groundwater
45 conditions (Bennett et al., 2016). Similar to deep seated landslides, earthflows can cause upstream channel aggradation and
46 valley widening; Nereson and Finnegan (2018) note an order of magnitude increase in valley width upstream of the Oak Ridge,
47 California, earthflow.

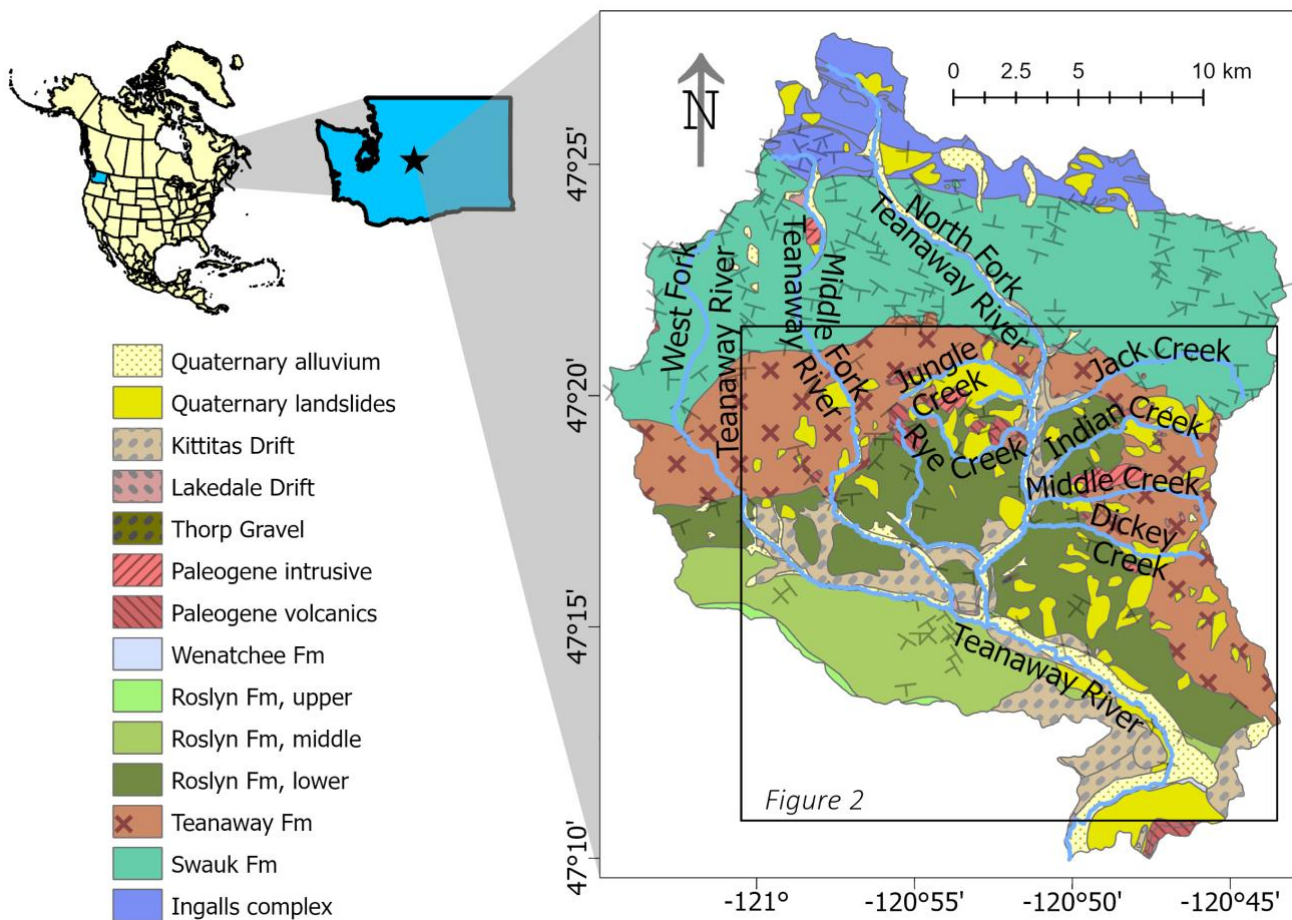
48

49 Due to their persistence, earthflows can be major sources of sediment to channels, and therefore a significant disturbance to
50 habitat and landscape evolution. For example, although earthflows in the Eel River basin, California, USA, cover only 6% of
51 the basin, they account for half of the regional denudation rate with approximately 19,000 t/km/yr of sediment produced
52 (Mackey and Roering, 2011). Additionally, in-stream sediment production from earthflows is unsteady because annual to
53 decadal precipitation conditions cause intermittent movement over the decades to centuries that the earthflow is active
54 (Guerriero et al., 2017; Mackey and Roering, 2011). Earthflows can temporarily transition to debris flows, resulting in rapid
55 transport of weathered material and debris to the channel (Malet et al., 2005). Differential erosion by earthflows results in
56 valley-scale topographic patterns: lithologic controls on earthflow location in the Eel River basin, California, USA,
57 concentrates erosion in the melange units, and lowers that landscape relative to isolated resistant sandstone outcrops (Mackey
58 and Roering, 2011).

59

60 Here, we examine the cause and timing of Holocene earthflows in the Teanaway Basin of the central Cascade Range of
61 Washington State, located in the northwest corner of the continental USA. Geologic mapping of the region and recent lidar
62 reveals extensive landsliding in the form of earthflows (Quantum Spatial, 2018, 2015; Tabor et al., 1982), but the cause and
63 timing of these earthflows is unknown. We develop a relative dating curve for earthflows and apply it to the Teanaway basin

64 to determine when the earthflows were active and discuss how earthflow activity affected valley width, sediment supply, and
65 habitat during the Holocene.



66
67 **Figure 1. Geologic map of the Teanaway watershed (Tabor et al., 1982) including strike and dip directions of geologic units. Upper**
68 **left inset shows location of Washington State in North America, and the location of the study area (star) within Washington State.**
69 **Box shows location of Figure 2.**

70 2 Study Site

71 The Teanaway River is located in central Washington State, northwest USA, four miles east of Cle Elum, WA (Figure 1). This
72 single-thread river has three main tributaries known as the West Fork, the Middle Fork, and the North Fork which all flow into
73 the main Teanaway River about 10 miles upstream of its confluence with the Yakima River. The region receives between 980
74 and 1230 mm of precipitation annually and is typically snow-covered during the winter (U.S. Geological Survey, 2012) with
75 large fires occurring every 300-350 years (Agee, 1996; 1994), though high-intensity burns are limited to less than 1 km²
76 (Wright and Agee, 2004). Mapped faults do not offset Quaternary alluvium and exhumation and Holocene denudation rates
77 are low at 0.05 mm/yr and 0.08-0.17 mm/yr respectively (Moon et al., 2011; Reiners et al., 2003). The branches of the

78 Teanaway River were splash dammed from 1892-1916 (Cle Elum Tribune, 1891; Kittitas County Centennial Committee, 1989)
79 and the *Pinus ponderosa* forests were logged from the 1890s through the 1940s. As a result of anthropogenic logging practices,
80 forests in the study area are less than 100 years old, and stream channels in the Middle and West Forks have incised up to 2
81 meters through bedrock (Schanz et al., 2019).

82

83 The majority of rock units in the study area were deposited during the Eocene (Figure 1). The lower Eocene Swauk Formation,
84 composed of dark sandstone with small amounts of siltstone and conglomerate, unconformably overlies the Jurassic Ingalls
85 Complex and is ~4800 m thick (Tabor et al., 1984). The Swauk Formation is folded with dip directions generally to the south
86 (Tabor et al., 1982). The middle Eocene Teanaway Formation unconformably lies on the steeply tilted Swauk Formation. The
87 Teanaway Formation ranges from 10 to 2500 m thick and is composed of basaltic and andesitic lava flows interbedded with
88 tuff, breccia, and feldspathic sedimentary rocks (Tabor et al., 1984). Because of its resistance to weathering, this formation
89 forms most of the taller and more rugged peaks in the Teanaway area. Rhyolite flows from this formation have interbedded
90 with the conformable upper Eocene Roslyn Formation and outcrop through the study area as dikes (Tabor et al., 1984). The
91 youngest surficial rock unit, the Roslyn Formation, covers most of the lower-elevation study area. The unweathered white and
92 weathered yellow immature sandstones were deposited conformably on the Teanaway Formation in the late Eocene (Tabor et
93 al., 1984). The Roslyn and Teanaway formations lie relatively flat or gently tilted to the southwest compared to the Swauk
94 Formation, and are very susceptible to erosion and sliding due to the interbedded tuffs, paleosols, clays, and silts (NFTWA,
95 1996; Tabor et al., 1982).

96

97 Overlying the Eocene units are glacial and mass wasting deposits. Glacial terraces originate from the Thorp and Kittitas
98 glaciations at 600 ky and 120 ky, respectively (Porter, 1976). During drift deposition, glaciers from the Cle Elum catchment
99 to the west overtopped the dividing ridge and entered the West Fork and lower Middle and North Fork Teanaway valleys.
100 Thorp and Kittitas moraines, composed of poorly sorted gravels and cobbles, are present at the eastern edge of the study area
101 near the outlet of the mainstem Teanaway into the Yakima River and on the ridges surrounding the West Fork Teanaway
102 (Porter, 1976). The Thorp drift sediments are heavily eroded and therefore less visible than the Kittitas drift sediment, which
103 has been modified by mass wasting (Porter, 1976).

104

105 Geologic mapping has identified several Quaternary mass wasting deposits in the Roslyn and Teanaway formations (Figure 1)
106 and subsequent reports have focused on shallow landslides near stream banks (NFTWA, 1996). Landslides are as old as late
107 Pliocene and are concentrated near rhyolite tuffs and a weathered surface in the Teanaway Formation, which form planes of
108 weakness (NFTWA, 1996). Although closed depressions and ponds are visible in the lidar and suggest some recent activity,
109 landslides are not easily distinguished in aerial photography or in the field. Lidar in 2015 and 2018 (Quantum Spatial, 2018,
110 2015) revealed the extent of these slides, but no studies since have quantified landslide volumes, constrained the timing or
111 mechanism of sliding, or discussed the impact of the deep-seated landslides and earthflows on the landscape.

112 **3 Methods**

113 Our analysis focuses on the entirety of the Teanaway basin, though the majority of the earthflows are found within tributaries
114 to the North Fork Teanaway River. To identify the temporal and spatial distribution of earthflows, we use geomorphic mapping
115 in conjunction with a directional roughness metric to identify and relatively date earthflow activity in the Teanaway basin.
116 Other studies (e.g., Bennett et al., 2016; Mackey and Roering, 2011) use tree and object tracking to measure earthflow velocity;
117 we attempted to do this but found the dense vegetation and high tree growth rates prevented us from accurately matching
118 objects between image pairs. Thus, we rely on surface roughness to give relative earthflow activity. We test the relationship
119 between directional roughness and time since earthflow activity using a numerical model, and further constrain the relative
120 ages using radiocarbon and sedimentation ages, which both give maximum estimates of earthflow activity.

121 **3.1 Earthflow mapping and maximum earthflow ages**

122 We first created a detailed earthflow map for the study region. All visually-identifiable landslides within the Teanaway basin
123 were digitized in ArcGIS from one-meter resolution lidar (Quantum Spatial, 2018, 2015) at a scale of 1:5000. Earthflows were
124 classified from this dataset based on: hourglass shape with a wide head scarp and toe compared to a narrow transport zone,
125 narrow width and long length of slide zone, visible levees or shear zones at the edges, and flow-like morphologies (Baum et
126 al., 2003; Nereson and Finnegan, 2018). We mapped the edges of earthflows as the edge of shear zones next to undisturbed
127 hillslopes, and used scarps and toe deposits to delineate the top and bottom of earthflows from surrounding hillslopes. These
128 morphologic clues degrade over time and it becomes harder to distinguish earthflows from other mass movements. Therefore,
129 we focus our analysis on Holocene earthflow activity when it is still possible to distinguish the characteristic earthflow
130 morphologies.

131

132 We dated select earthflows using buried charcoal found within the earthflow toe deposits. Long residence times of buried
133 charcoal in landslides can result in radiocarbon ages >8000 years older than landslide activity (Struble et al., 2020); considering
134 that earthflows can also have episodic activity which further complicates the relationship between timing of earthflow activity
135 and radiocarbon age, we use our charcoal ages to loosely constrain maximum earthflow activity. Maximum earthflow activity
136 refers to a maximum estimate of how long since an individual earthflow first became active. Sampled earthflows were selected
137 based on potential for a fresh exposure via road or stream erosion and to capture a range of activity, which we estimated by
138 the prominence of levees and shear zones in the bare earth lidar. In the field, we removed 10-50 cm of material from the toes
139 of earthflows exposed by stream cuts or roadcuts to find 2-5 grams of charcoal (Figure S1 in the Supplement). We collected
140 radiocarbon samples from seven different earthflows (Table 1); one sample (8-4-20-2) did not yield enough carbon material
141 to date. The samples were sent to the Center for Applied Isotope Studies (CAIS) lab at the University of Georgia and were
142 dated using Accelerated Mass Spectrometry (AMS); dates were calibrated to calendar years using Intcal20 (Reimer et al.,
143 2020).

144

145 In three cases where earthflows dammed the valley and formed lakes, we estimated the onset of valley blockage, and thus an
146 estimate for when earthflow activity began, by using the sedimentation age of the lake. We reconstructed a pre-earthflow valley
147 bottom using the techniques in Struble et al. (2020). We estimated the valley bottom elevation under the lakes using the average
148 valley slope of surrounding un-dammed valleys. This valley floor estimate is interpolated in GIS with the lake perimeter
149 elevation to form an estimated lake bottom topography. The bottom topography is subtracted from the lidar surface elevation
150 to estimate the sedimentation volume post-earthflow. We used nearby mid-Holocene ¹⁰Be denudation rates of 0.08 and 0.17
151 mm/yr (Moon et al., 2011) from neighbouring basins with similar mean annual precipitation and glaciation. We multiplied the
152 denudation rates by upstream contributing area for each lake to give a volumetric estimate of sediment delivery per year. The
153 lake sedimentation volume is divided by this rate to estimate the years necessary to fill each lake. We repeat this process with
154 the upper and lower denudation bounds to give a range of plausible sedimentation ages, which approximate when the earthflow
155 dammed the creek. Earthflow activity may continue after lake formation; thus, these sedimentation ages do not necessarily
156 represent the most recent earthflow activity.

157 **3.2 Estimating earthflow activity using flow directional surface roughness**

158 To relatively date earthflow activity, we created a surface roughness age calibration model similar to that used to date rotational
159 slides in Washington State (LaHusen et al., 2016; Booth et al., 2017). Active earthflows have a unidirectional flow morphology
160 that gradually diffuses to less directional roughness as activity ceases, in contrast to rotational slides which start with uneven
161 roughness in all directions. To account for the unique flow morphology of earthflows, we used a flow directional Median
162 Absolute Differences (MAD) index (Trevisani and Rocca, 2015). MAD is a bivariate geostatistical index that analyzes residual
163 elevations between paired locations in a Digital Elevation Model (DEM) (Trevisani and Cavalli, 2016). MAD results in a
164 roughness index for each direction (N-S, E-W, NE-SW, and NW-SE) across each raster cell in the study area. Using surface
165 flow directions derived from the DEM surface, these directional roughnesses are filtered to correspond to the flow direction;
166 e.g., if the surface flow direction is N-S, then only the N-S roughness is used (Trevisani and Cavalli, 2016). A high MAD value
167 represents topographic roughness in the direction of flow, while a low MAD represents relatively smooth regions.

168

169 MAD is calculated using the residual roughness to filter out large-scale topographic variations; we first smoothed the one-
170 meter DEM over a 3x3 window followed by a 5x5 window (Trevisani and Cavalli, 2016) and subtracted the smoothed DEM
171 from the original DEM to obtain a raster of residual roughness elements (Figures S2 and S3 in the Supplement). The MAD
172 index (<https://github.com/cageo/Trevisani-2015>) was run with this residual raster and calculated the directional roughness over
173 an 8 m radius window. We chose this window so that we examine a similar spatial scale as the 15x15 window used by LaHusen
174 et al. (2016). We calculated flow direction across the smoothed DEM and created a raster with the MAD values in the direction
175 of flow for each cell. Finally, we used Zonal Statistics to calculate the standard deviation of the directional roughness (MADstd)

176 for each earthflow; from our diffusion model simulations (see below), MADstd had the highest correlation with age ($R^2 =$
177 0.98).

178

179 The MADstd relative dating method rests on the assumption that earthflow MADstd will decrease with time since last
180 earthflow activity due to soil diffusion. In order to test this assumption, we simulated landscape diffusion on a recent earthflow
181 and calculated MADstd through time; if our assumption is correct, MADstd should decrease with simulation time. We
182 extracted elevations from an earthflow along Jungle Creek where we obtained radiocarbon sample 8-1-20-1 (Figure 2, Table
183 1). We chose this earthflow because it has clear flow lines and blocks the majority of the stream valley with an outlet eroded
184 through. This suggests the earthflow has been active recently to block the valley. We applied two-dimensional diffusion to the
185 earthflow surface, based on Eq (1):

$$186 \frac{dz}{dt} = -K \frac{dz^2}{dx^2}, \quad (1)$$

187 where dz is change in elevation, dt is the timestep, and dx is the spatial resolution. The diffusion rate, K , is estimated as 0.002
188 m^2/yr based on regions in a similar climate (Martin, 2000), though we varied diffusion rate as low as 0.0002 m^2/yr for
189 landscapes experiencing creep (Martin, 2000). We also ran the diffusion model with and without stream erosion. Stream
190 erosion is represented by Eq (2):

$$191 \frac{dz}{dt} = K_{sp} A^m S^n, \quad (2)$$

192 where A is the upstream contributing drainage area, S is slope, and K_{sp} , m , and n are empirical coefficients related to drainage
193 basin geometry, rock erodibility, channel hydraulics, and climate (Braun and Willett, 2013). The values of m and n are set at
194 0.5 and 1, respectively, based on common values for mountain streams (Braun and Willett, 2013), and K_{sp} is estimated at 6e-
195 7 from empirical relationships between average denudation (Moon et al., 2011), A , and S along Jungle Creek. We ran the
196 diffusion model for 10 ky and calculated MAD every 2 ky.

197

198 3.3 Valley width

199 To examine the influence of landslides on habitat, we measured valley width along the tributaries of the North Fork Teanaway.
200 Valley width typically increases with increasing drainage area in a power law relationship of form:

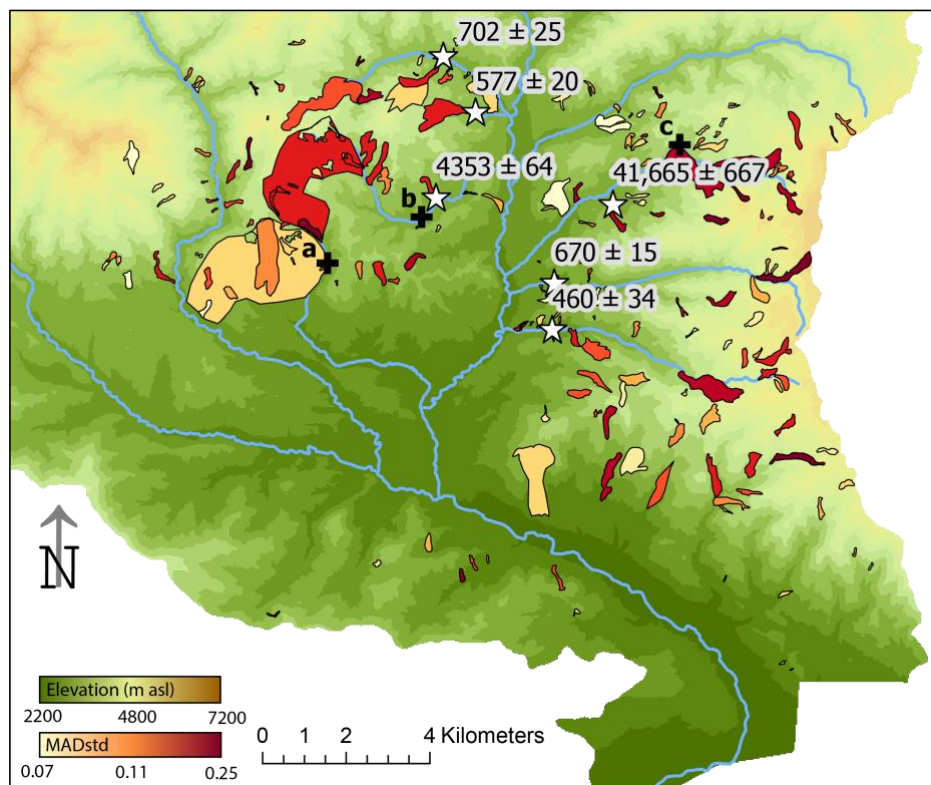
$$201 W_v = aA^b, \quad (3)$$

202 Where W_v is valley width, a and b are empirical parameters, and A is upstream drainage area. In the Washington and Oregon
203 Coast Ranges within similar sedimentary rocks as the Roslyn Formation but in a wetter climate, a is 67 and b is 0.34 (Schanz
204 and Montgomery, 2016) for a landscape lacking deep-seated landslides or earthflows. Similar values for b are found across
205 the tectonically quiescent Appalachian Plateau, USA (Clubb et al., 2022).

206

207 In order to isolate the effect of earthflows on valley width, we focus on tributary valleys of the North Fork. The mainstem and
208 three forks of the Teanaway all have wide valleys that are unaffected by earthflows. In contrast, the tributary valleys of the
209 North Fork are altered by earthflows. We extracted valley width from Jungle, Rye, Dickey, Middle, Indian, Jack, and an
210 unnamed creek (Figure 1) by defining the valley floor as being less than 5% slope. We used an automated process in ArcGIS
211 to extract a valley centerline, create transects every 100 m, and measure valley width as the width of the transect line within
212 the 5% valley slope.

213



214

215 **Figure 2. Earthflows mapped in the study area; earthflows are colored by their MADstd value. Radiocarbon locations and dates, in**
216 **calibrated yr BP, are shown with white stars. Black crosses indicate locations of earthflow-dammed lakes where sedimentation ages**
217 **are derived: a – unnamed creek; b – Rye Creek; and c – Indian Creek. Extent of region is shown in Figure 1. Background elevation**
218 **data from Quantum Spatial (2015; 2018).**

219 **4 Results**

220 We present the results of earthflow mapping and dating below. In order to verify the relative dating method, we first present
221 earthflow mapping, valley width, and maximum age estimate results, then use those results and the diffusion simulations to
222 test how well the MADstd relative dating works. Finally, we conclude with a basin-wide perspective on the timing of
223 earthflows based on MADstd values.

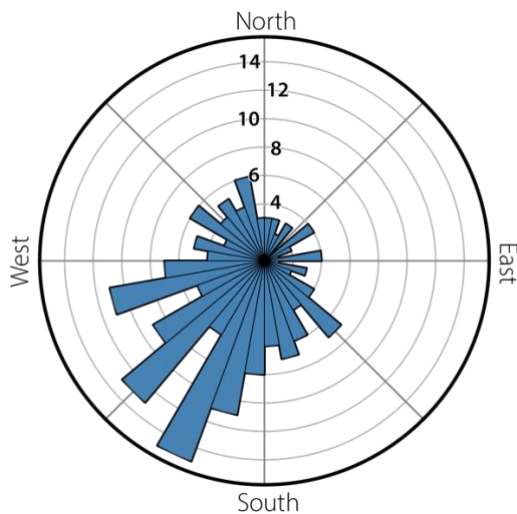
224 4.1 Earthflow mapping

225 We mapped 187 earthflows in the lower Teanaway basin (Figure 2). Earthflows range in size from 1076 m² to earthflow
226 complexes 4e6 m² in area with a median area of 28,547 m². Mapped earthflows are mostly all north of the mainstem and
227 Middle Fork of the Teanaway River, with the exception of eight small earthflows south of the Main Fork. The southern edge
228 of the earthflow area appears to be bound by the extent of Pleistocene glaciation (Figure 1); perhaps glaciation removed pre-
229 existing earthflows or the muted topography from glacial erosion is less prone to mass movement. To the north, the earthflow
230 domain is bound by the start of the Swauk Formation, which has little to no mappable landslides in it.

231

232 Earthflows spatially cluster in the Teanaway and lower Roslyn formation. Just over half (51%) of mapped earthflows are in
233 the Teanaway Formation, which is composed of basalt and rhyolite interbedded flows and conformably grades upwards into
234 the lower Roslyn Formation, in which 42% of earthflows are found. The remaining 7% are split between the Swauk and middle
235 Roslyn Formations.

236



237

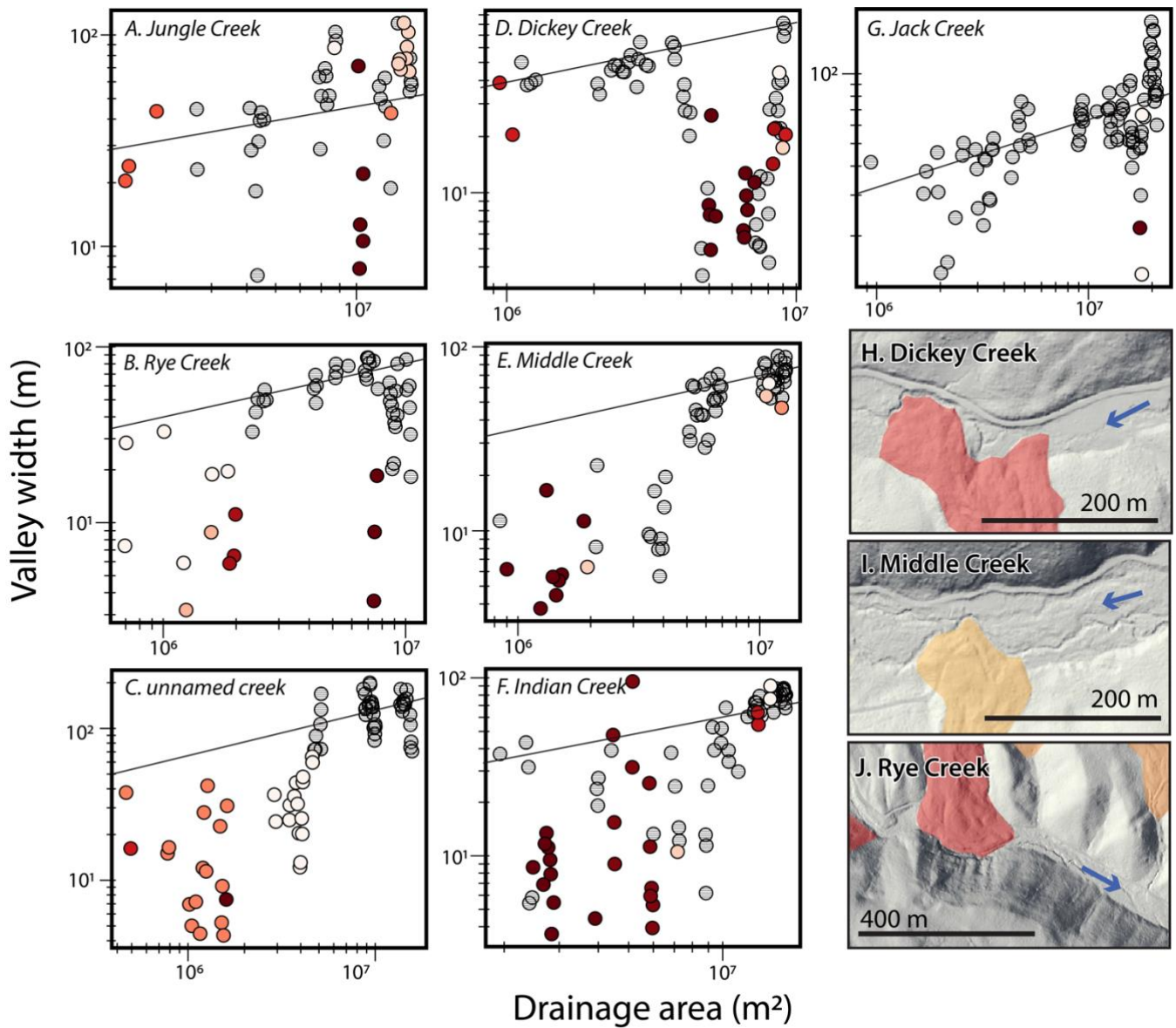
238 **Figure 3. Average earthflow aspect, binned by 10 degrees. Contours indicate number of earthflows in each bin.**

239

240 We extracted slope and aspect for each earthflow. The slope distribution, measured based on the smoothed one-meter lidar,
241 was similar between earthflows and intact hillslopes of the Lower and Middle Roslyn Formations with modal slopes of 10 to
242 15 degrees. The average earthflow aspect shows strong preference for the southwest quadrant, with 45% of earthflows (Figure
243 3). The northwest and southeast quadrants were similarly populated with 20 and 21%, respectively, while the remaining
244 earthflows are found in the northeast quadrant.

245

246



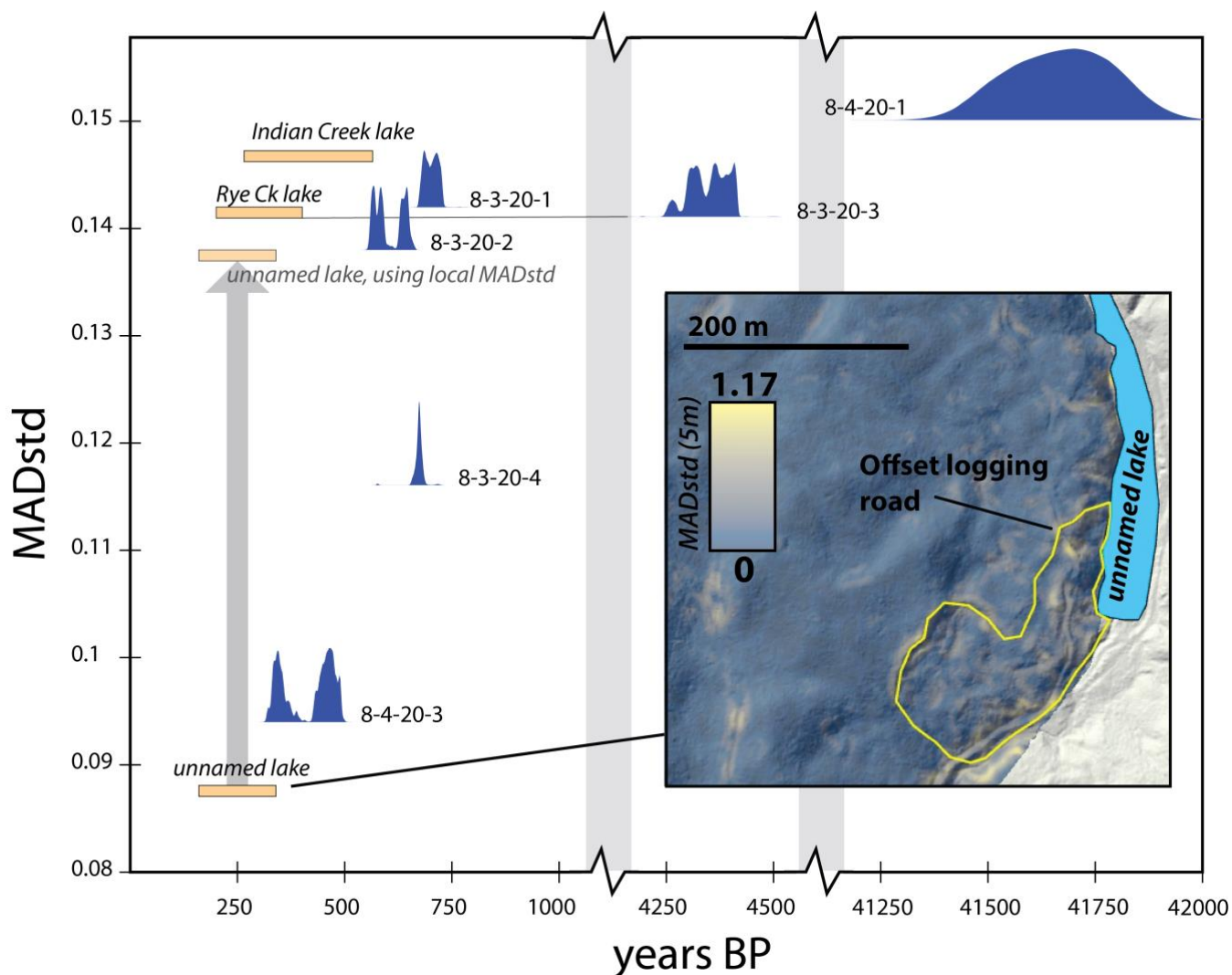
247

248 **Figure 4. Valley width of the North Fork tributaries compared to upstream contributing drainage area (A-G). Black lines show a**
 249 **power law relationship with exponent 0.3 (Schanz and Montgomery, 2016; Clubb et al., 2022). Tributaries are arranged counter**
 250 **clockwise from the northwest (see Figure 1 for locations). Colored circles indicate valley width measurements where one valley wall**
 251 **is an earthflow; colors reflect MADstd relative to earthflows within that tributary in which red are high MADstd and light pink are**
 252 **low MADstd. Panels H-J show examples of earthflows interacting with valley bottoms; earthflow color corresponds to MADstd value**
 253 **using same color scheme as panels A-G. Blue arrows show direction of water flow.**

254 4.2 Valley width

255 Valley width generally increases with drainage area for the seven tributaries we examined, although the increase is not
 256 consistent (Figure 4). Jungle Creek has its narrowest width, equivalent to the channel width, halfway up the valley where a

257 high MADstd earthflow pinches the valley. The valley width immediately upstream is 100 m wide, comparable to the widest
 258 part of the valley at the mouth of Jungle Creek. Similarly, Rye Creek's valley is pinched to the channel width at 2 km upstream
 259 (drainage area = 7.5e6 m²) and widens immediately upstream to the widest values noted along the tributary. Similar trends of
 260 narrowed valleys with wider sections immediately upstream are seen in the other tributaries, though the trends are less strong.
 261 Rye, Middle, Indian, and the unnamed creek are confined by earthflows in the upper 1-2 km; these earthflows form the valley
 262 walls and bottom and constrain the valley width to the active channel width.
 263



264
 265 **Figure 5. Comparison of maximum age estimates and MADstd values. Range of maximum earthflow ages from lake sedimentation**
 266 **are shown as orange bars and radiocarbon ages are shown with blue probability distribution functions. Inset shows the MADstd**
 267 **values calculated with a 5m moving window for the earthflow complex creating the unnamed lake. Note the relatively low MADstd**
 268 **in blue despite dense *Pinus ponderosa* forest covering earthflow surface. Yellow outline shows a possible re-activation of part of the**
 269 **complex, which raises the MADstd associated with lake formation from 0.087 to 0.137.**

270 4.3 Maximum earthflow ages

271 Age results from radiocarbon dating range from 370 to 36,750 carbon-14 years before present, or 460 ± 34 to $41,665 \pm 237$
272 calibrated years before present (yr BP) (Table 1, Figure 5). Samples were taken from the toe of earthflows, and represent
273 charcoal that was originally deposited in regolith then transported through earthflow movement. Thus, the age given by
274 radiocarbon dating is a measure of 1) the inherited age of the charcoal, 2) regolith development, 3) earthflow transport, and 4)
275 deposition at the earthflow toe. We cannot use our ages to directly date the last earthflow activity, but it does provide a
276 maximum estimate of earthflow age.

277

278 Based on a range of denudation rates of 0.08 to 0.17 mm/yr, the lake formed along Indian Creek (Figure 2) took approximately
279 267 to 567 years to fill to the current level (Figure 5), indicating the earthflow has been constricting Indian Creek for at least
280 that long. The lake along Rye Creek, formed just upstream of earthflow carbon site 8-3-20-3, took between 204 and 433 years
281 to fill with sediment to the modern level, and the lake along the unnamed creek took approximately 159 to 337 years to fill.

282

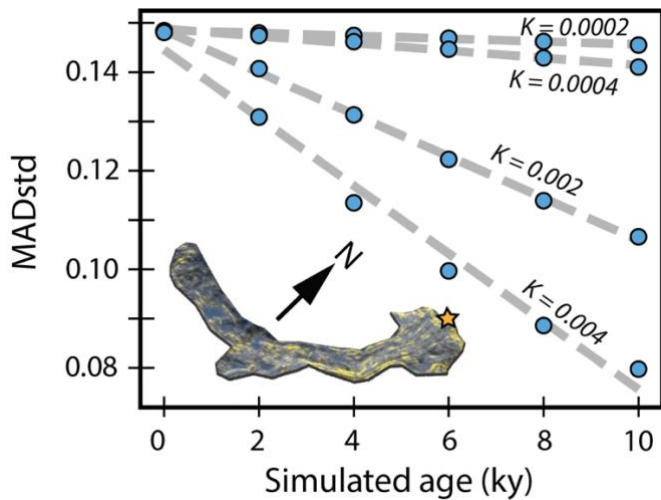
283 The ages we derived from sedimentation rates and lake volume do not directly date earthflow activity, though the relationship
284 is more complex than the radiocarbon ages. The lake itself formed when the earthflow initially dammed the valley, and so
285 represents a maximum age – or a near maximum age if earthflow velocity was slower and did not immediately dam the channel.
286 However, all lakes are currently filled with sediment and an outlet stream has eroded through the damming earthflow, which
287 indicates the sedimentation age is a minimum estimate of the lake's age. Based on the observation that the outlet stream is
288 still forming a knickpoint in the earthflow and has not yet incised through the lake fill, we believe the sedimentation age is
289 close to the age of the lake and thus these ages more closely estimate the maximum earthflow age.

290

291 We were able to get a radiocarbon age and a sedimentation age for one earthflow: the Rye Creek earthflow was dated with
292 charcoal to 4353 yr BP but has a sedimentation age of 204 to 433 years. These ages indicate upwards of 4000 years of residence
293 time for charcoal in the earthflow, similar to values found for rotational landslides in the Oregon Coast Range (Struble et al.,
294 2020), and a maximum estimate of earthflow activity to approximately 204 to 433 years ago. The other earthflows creating
295 lakes are similarly young, with maximum ages in the last 500 years; radiocarbon ages support relatively recent earthflow
296 activity with maximum age estimates of less than 1000 years for four of the six dated earthflows.

297

298



299

300 **Figure 6. MADstd values for simulated diffusion across the Jungle Creek earthflow. Inset images shows the Jungle Creek slide with**
 301 **modern (simulation time = 0) MAD values where yellow are high directional MAD and blue are low. Star shows location of sample**
 302 **8-3-20-1. For all diffusion values, linear regressions give an r-squared of >0.98.**

303

Table 1. Radiocarbon dates

Lab ID	Tributary name	Latitude	Longitude	C-14 yrs BP (2 sigma)	calibrated yr BP (2 sigma)	MAD std
8-3-20-1	Jungle Creek	47.34689	-120.87804	790 ± 20	702 ± 25	0.142
8-3-20-2	unnamed tributary to Jungle Creek	47.33463	-120.87036	640 ± 20	577 ± 20 (p = 0.57)	0.138
					643 ± 18 (p = 0.43)	
8-3-20-3	Rye Creek	47.31456	-120.87959	3910 ± 20	4353 ± 64	0.141
8-3-20-4	Middle Creek	47.29731	-120.84273	73 0 ± 20	670 ± 15	0.116
8-4-20-1	Indian Creek	47.31481	-120.82517	36750 ± 20	41665 ± 237	0.15
8-4-20-3	Dickey Creek	47.28752	-120.84302	370 ± 20	460 ± 34 (p = 0.61)	0.094
					349 ± 29 (p = 0.39)	

304

305 4.4 Verification of MADstd relative dating

306 Simulated diffusion verified our assumption that MADstd decreases with time since earthflow activity. The Jungle Creek
 307 earthflow shows a strong linear relationship between MADstd and earthflow age (Figure 6) with an r-squared fit of >0.98 for
 308 all four hillslope diffusion values tested. When simulations were run with stream erosion, resulting MADstd values were very
 309 similar with less than 5% difference in values and a median difference of 0.2%. Therefore, whether stream erosion is considered
 310 or not is negligible to the MADstd value. The linear decrease in MADstd values with time supports our initial theory that as

311 earthflows stop moving, the directional roughness becomes more similar across the earthflow surface. Soil diffusion creates a
312 more multi-directional surface with lower variation in flow directional roughness. When earthflows are active, orthogonal flow
313 off the flow features and scarps creates a highly variable MAD and thus a high MADstd.

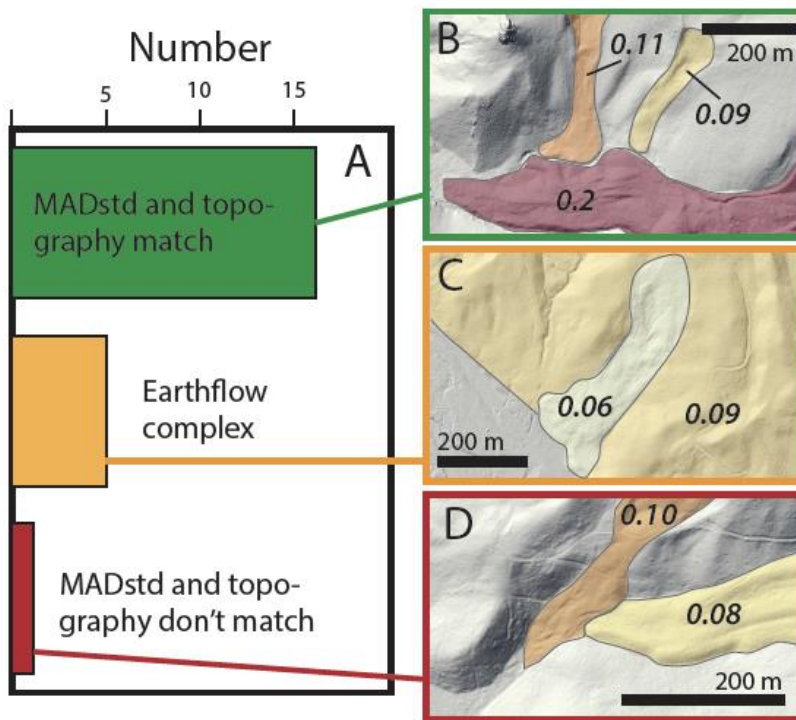
314

315 While our simulations give equations relating age and MADstd, we do not apply this equation to the study area because the
316 relationship is highly dependent on the soil diffusion value and on earthflow velocity, which would affect the relative strength
317 of diffusive versus advective processes. We do not know the site-specific diffusion rate, and even slight differences between
318 $K = 0.0002$ and 0.0004 give widely different age estimates (Figure 6). We also do not know how the diffusion rate changed
319 over the late Quaternary in our study area. However, we can assume that the diffusion rate and associated variations are similar
320 across our study area, where climatic and biotic forcings are relatively uniform and earthflow source lithology is either lower
321 Roslyn or Teanaway formation. Thus, we should be able to use MADstd to relatively date earthflow activity.

322

323 When we apply the MADstd metric to mapped earthflows (Figure 2), topographic relationships support the relative dating
324 technique (Figure 7). In our study area, there are 22 instances of earthflows clearly overlapping with another, in which
325 morphologic clues can be used to relatively date them. Of these, 16 had MADstd values consistent with the cross-cutting
326 relationship where the on-lapping earthflow had higher MADstd values than the underlying earthflow. In cases where the
327 MADstd gave incorrect relative ages, five were on earthflow complexes. MADstd appears to not work as well across large
328 earthflow complexes where there is more heterogeneity in activity and less defined flow lines and scarps. If we disregard
329 earthflow complexes, then only one of 17 cross-cutting relationships is not consistent with the relative MADstd values.

330



331

332 **Figure 7. A) Cross cutting relationships compared to MADstd relative age relationships and B-D) examples of cross cutting**
 333 **relationships underlain by a lidar hillshade (Quantum Spatial, 2015; 2018). B) shows two examples where the higher MADstd**
 334 **earthflow topographically truncates two lower MADstd earthflows. C) shows an example where the MADstd relative dating does**
 335 **not work, in which the cross-cutting earthflow has a lower MADstd than the earthflow complex it sits within. D) is an example where**
 336 **the toe of a lower MADstd earthflow onlaps a higher MADstd earthflow, indicating a mismatch between MADstd and topography.**
 337 **Numbers indicate the MADstd value for each earthflow, which is also reflected by the earthflow color, using the same color**
 338 **scheme as Figure 2.**

339

340 Valley bottom impingement also supports the MADstd relative ages. Active earthflows are more likely to block tributary
 341 valleys in contrast to older, less active earthflows whose deposits can be eroded by the stream to re-form a wide valley.
 342 Earthflows that completely block valleys, or narrow valleys to the channel width, have higher MADstd values than earthflows
 343 that only partially block valleys (Figure 4H-J). Earthflows with low MADstd values are near the regression line for non-
 344 landslide terrain, suggesting their toes have been eroded to the valley walls (Figure 4). One outlier to this is the 4-6 kilometers
 345 along Rye Creek and the unnamed creek (Figure 4B, C) with a low MADstd but strong effect on valley width. Both of these
 346 earthflows are large earthflow complexes (3-4 km²) and the MADstd value of the entire complex may not represent the locally
 347 active portions that affect the two creeks.

348

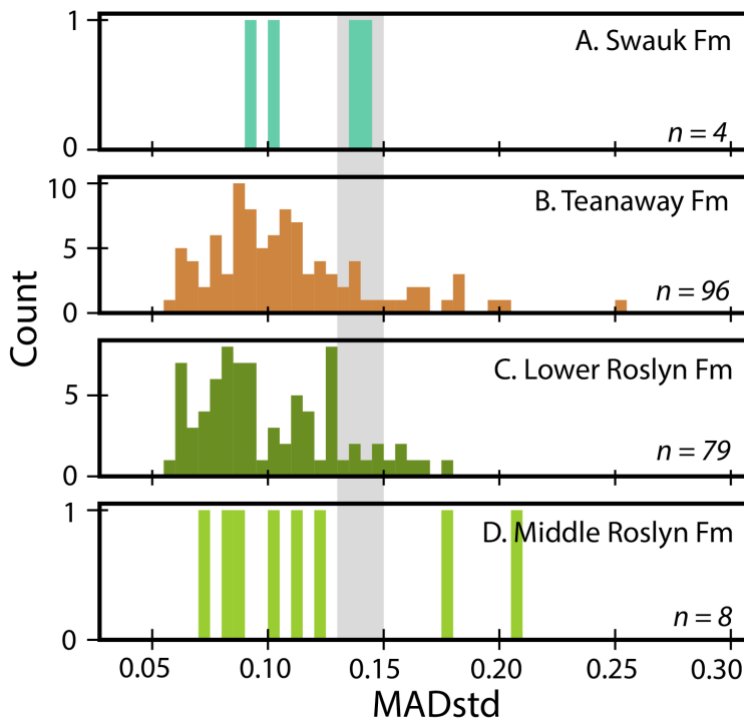
349 Although MADstd appears to work to relatively date earthflows across the study area, comparing lake sedimentation ages and
 350 MADstd indicates that earthflows active at a similar time may display a range of MADstd values. Lakes along Rye and Indian

351 Creek have sedimentation ages of 204 to 433 and 267 to 567 years, respectively, with MADstd values of associated valley-
352 blocking earthflows of 0.141 and 0.146 (Figure 5). Given the error in sedimentation ages, we consider these lakes to have
353 formed at approximately the same time, thus indicating that MADstd values can range by at least 0.005 for earthflows with
354 similar activity history.

355

356 The sedimentation age for the lake along the unnamed creek is an outlier, with the youngest range of sedimentation ages (159
357 to 337 years) yet the lowest MADstd of 0.087 which represents the least active earthflow of the three studied lakes. The 0.087
358 value comes from a large earthflow complex that borders the western and southern edge of the lake. When MADstd is
359 calculated using a moving window of 5m, variations in MADstd across the earthflow complex become clear (Figure 5 inset).
360 In particular, a higher MADstd region can be identified at the base of the lake, where a sharper headscarp and an offset logging
361 road indicate reactivation of this part of the earthflow complex. The MADstd of the reactivated portion is 0.137, much higher
362 than the 0.087 value for the earthflow complex as a whole. When the new value is used, we see that the three lakes cluster in
363 a range of MADstd values of 0.137 to 0.146 with an age of approximately 250-500 years. Therefore, we conclude that
364 earthflows active in the last few hundred years may have a range of MADstd of 0.137 to 0.146. When relatively dating
365 earthflow activity, we should use MADstd differences of >0.01 to differentiate separate periods of earthflow activity.

366



367

368 **Figure 8. Distribution of MADstd values by lithology, binned by 0.05. Grey bars show the MADstd range 0.13 to 0.15 that is**
369 **associated with recently active earthflows.**

370 **4.5 Relative earthflow activity**

371 Now that constraints on MADstd usage are determined, we analyze patterns in relative earthflow age by underlying lithology.
372 Soil diffusion is the primary control on the relationship between MADstd and earthflow activity (Figure 6); diffusion is set by
373 climate (Sweeney et al., 2015) and lithology (Johnstone and Hilley, 2015) which determine the rate of soil movement as well
374 as soil thickness. The study area experiences similar climate, and so we can compare earthflows within each lithologic unit to
375 contrast relative earthflow activity.

376

377 Only five and eight earthflows are sourced in the Swauk or Middle Roslyn formations, respectively, and MADstd values range
378 from 0.07 to 0.21 (Figure 6). The majority of earthflows (n=96) are underlain by the volcanic Teanaway Formation. MADstd
379 values are clustered around 0.10, with a small frequency peak near 0.17. Unlike the mostly unimodal distribution in the
380 Teanaway Formation, earthflows in the lower Roslyn Formation have a bimodal MADstd distribution with peaks at 0.08 and
381 0.13.

382

383 Absolute ages suggest that earthflows active in the last few hundred years have MADstd values of 0.13 to 0.15, approximately
384 (Figure 5), and that differences of >0.01 MADstd are necessary to distinguish between relative earthflow ages. Based on this,
385 the earthflows underlain by the Teanaway Formation are mostly inactive but do contain some earthflows that have been active
386 in the last few hundred years; 24 (25%) earthflows have MADstd of >0.13. For earthflows underlain by the Roslyn Formation,
387 a similar percentage were likely active in the last few hundred years, with 20 (25%) earthflows with a MADstd of >0.13.

388

389 That the MADstd values for the lower Roslyn Formation are bimodal indicates the prevalence of active earthflows with
390 MADstd of >0.13 is unlikely to be due to a preservation bias, nor to constant earthflow activity. Instead, the sharp break
391 between active earthflows and the cluster of older earthflows around 0.08 MADstd suggests a history of: initial earthflow
392 activity, followed by a cessation in which soil diffusion acted across earthflows, then re-activation or new earthflow formation
393 of 25% of the earthflows in the study area.

394 **5 Discussion**

395 **5.1 Drivers of earthflow motion**

396 Our aspect analysis showed a strong preference for earthflows to be oriented towards the southwest quadrangle (Figure 3), and
397 we hypothesize that this reflects a bedding plane control on earthflow location. The Roslyn and Teanaway Formations are
398 gently dipping to the southwest (Figure 1) with dip angles ranging from 10 to 30 degrees (Tabor et al., 1982), comparable to
399 the modal and median earthflow slopes. There is some variability in the bedding orientation as the Teanaway and Roslyn
400 formations curve to the west, but only 8.5 percent of earthflows by area are located in this southeast-dipping region. Southeast

401 aspects account for 21% of mapped earthflows; this mismatch implies not all earthflows are directly aligned to underlying
402 bedding planes. Possibly, southerly aspects could be preferential due to vegetation and evaporation conditions that affects
403 hillslope stabilization. However, the hillslopes in our study area are uniformly *Pinus ponderosa* dominated forest. The
404 preponderance of SW facing earthflows thus indicates that most earthflows are lithologically controlled. Since the Roslyn and
405 Teanaway are conformable, the bedding plane orientation also reflects the mid-Eocene landscape surface, and therefore the
406 orientation of paleosols within the two units. Previous work has noted that paleosols and volcanic flows interspersed in the
407 Teanaway and Roslyn formations form planes of weakness for landslides (NFTWA, 1996). That our observed slopes and
408 aspects match the bedding orientation supports this finding and indicates the bedding provides a first-hand control on the
409 orientation of earthflows in the Teanaway basin.

410

411 Further support for a lithologic control is the prevalence of earthflows in the Teanaway and lower Roslyn Formations, with
412 94% of mapped earthflows in these two units that make up 32.7% of the study area. The southern edge of mapped earthflows
413 does align with the extent of Pleistocene glaciations, which overtopped the western drainage boundary and flowed in through
414 the West Fork Teanaway. Although earthflows likely postdate the 120ky glaciation, the muted topography resulting from
415 glacial erosion may be less prone to earthflows. The glacial extent overlaps both the middle and lower Roslyn Formation
416 (Figure 2), and earthflows in the lower Roslyn Formation stop at the low relief topography left by glacial erosion. Thus, glacial
417 erosion, in addition to underlying lithology, appears to control the extent of earthflow activity. At the southern edges of the
418 study area, glacial erosion is minimal and topographic relief increases. However, only eight small earthflows were mapped in
419 this region, which is underlain by middle and upper Roslyn Formation. Although conformable, the middle and upper Roslyn
420 Formation members lack rhyolite interbeds and are finer grained in comparison to the lower member (Tabor et al., 1984).
421 Likely, the interbedded rhyolite allows planes of weakness to form (NFTWA, 1996) that promote earthflow formation.

422

423 Our absolute and relative ages indicate approximately 25% (n = 46) of the mapped earthflows were active within the last few
424 hundred years; however, we do not have strong age control for the remaining 141 earthflows. Earthflow activity is often
425 correlated to climate (Bennett et al., 2016), with wetter periods driving earthflow motion (Baum et al., 2003) and drier periods
426 creating desiccation cracks that prime the landscape for deep water infiltration (McSaveney and Griffiths, 1987). The last few
427 hundred years in the Teanaway basin were climatically characterized by the Little Ice Age, which caused about 1°C cooler
428 conditions (Graumlich and Brubaker, 1986). This temperature change is unlikely to significantly alter weathering rates and
429 regolith production (Marshall et al., 2015; Schanz et al., 2019), and precipitation rates remained low. However, human
430 modification since 1890 may have contributed to earthflow activity. Starting c 1890, large scale deforestation and road building
431 began (Kittitas County Centennial Committee, 1989), which would decrease evapotranspiration and root strength, leading to
432 greater water infiltration and weaker soil cohesion; conditions that promote earthflow movement. Similar patterns are seen in
433 the Waipaoa River basin, New Zealand, where deforestation in the last two hundred years has resulted in mass movements and
434 increased sediment loads (Cerovski-Darriau and Roering, 2016).

435 **5.2 Landscape disturbance**

436 Earthflows in the Teanaway basin alter valley bottom topography and hillslope erosion rates, which affects habitat zones and
437 Holocene denudation rates. In the Teanaway forks and mainstem, no earthflows encroach on the valley bottoms, but all of the
438 North Fork tributaries examined in Figure 4 initiate on an earthflow or earthflow complex, with the exception of Jack and
439 Dickey creeks. Only a relatively small number (10 of 187) of mapped earthflows in the North Fork tributaries are in direct
440 contact with streams; these earthflows range in size from a large earthflow complex of 4 km² to smaller flows of 14,000 m²
441 and show mostly recent (<200 years) activity.

442

443 Increased sediment flux from earthflows appears to be mostly fine sediment; grain size surveys indicate high amounts of fine
444 sediment and moderate coarse sediment loads in the North Fork tributaries with no significant difference between tributaries
445 draining Teanaway and lower Roslyn formations, despite a rock strength difference between the basalt and friable sandstone
446 (NFTWA, 1996). In a similar sandstone formation, Fratkin et al. (2020) found significant variation in surface and subsurface
447 grain size when compared to adjacent tributaries draining basalt; most bedload in their study area was delivered by debris
448 flows and landslides. However, earthflows tend to incorporate highly weathered material and regolith; in the Eel River, 90%
449 of earthflow colluvium is smaller than 76 mm (Mackey and Roering, 2011). Field observations in the Teanaway at earthflow
450 toes and exposed surfaces were of sand and silt size fractions, with a few small gravels (Figure S1 in the Supplement), even at
451 radiocarbon site 8-4-20-2, which had insufficient carbon to produce an age but is from an earthflow sourced entirely from the
452 Teanaway Formation basalt. Thus, the abundant fine sediment and lack of significant grain size difference between tributaries
453 in the Teanaway and lower Roslyn formation may reflect large sediment contributions from earthflows, which preferentially
454 transport weathered regolith.

455

456 These effects on sediment flux and valley width are likely to disturb in-stream habitat. Heighted fine sediment delivery can
457 clog pore spaces in spawning gravels; however, channel slopes in the Teanaway basin are high and sufficient to quickly
458 transport sands and finer material downstream (NFTWA, 1996; Schanz et al., 2019). Floodplain habitat is reduced where
459 earthflows narrow the valley (Figure 4), though valley widths are abnormally large just upstream of earthflows in Jungle, Rye
460 and Dickey creeks. Valley width is a key landscape characteristic for salmon habitat (Burnett et al., 2007) and wider valleys
461 are often associated with heterogeneous channel features (Montgomery and Buffington, 1997) and flood refuge habitat (May
462 et al., 2013). That Teanaway earthflows can create heterogeneity in valley widths implies they exert a direct influence on
463 riparian habitat.

464 **5.3 MADstd as relative dating tool**

465 Our lake sedimentation ages showed very little relationship between MADstd and earthflow activity for recent earthflows;
466 however, this finding is consistent with other studies of landslide surface roughness. Comparing three surface roughness

467 metrics on landslides spanning ~200 years of activity, Goetz et al. (2014) found no relationship between surface roughness
468 and age. Booth et al. (2017) suggest surface roughness is more appropriately used to distinguish landslide ages at the scale of
469 thousands of years. Thus, the limitations of MADstd are similar to other surface roughness metrics in that we cannot distinguish
470 relative earthflow activity of <200 years.

471

472 Yet, MADstd is able to identify flow features and differentiate between forest terrain, which gives it an advantage over some
473 other roughness metrics. The original flow directional MAD metric picks up flow features such as scarps, debris flows, and
474 channels that are missed by isotropic roughness metrics (Trevisani and Cavalli, 2016). In the case of earthflows, high and low
475 flow directional MAD values are associated with the strong lineations; as flow follows the crests and hollows, the >1 m
476 lineations also direct flow orthogonal to crests (Figure 6 inset). By taking the standard deviation, we can highlight the parallel
477 and orthogonal flow that is characteristic of >1 m scale lineations; however, it is important to note that this method would not
478 work if the elevation model resolution is greater than the lineation scale. Compared to other metrics applied to landslides, the
479 MADstd includes a flow directional roughness and detrends the data, both of which have been found to improve landslide
480 identification accuracy (Berti et al., 2013; McKean and Roering, 2004). Previously used surface roughness metrics often have
481 trouble capturing the top of earthflows and differentiating between rough, forested terrain and landslide roughness (Berti et
482 al., 2013). When the MADstd is calculated over a moving 5 m radius window, rather than over a single earthflow, forested
483 hillslopes are clearly delineated from earthflows. The roughness elements from trees are isotropic and give MADstd values
484 near zero (Figure 5 inset). The scarp, flowlines, and toe produce strong lineations in the landscape that light up in the MADstd
485 plots, due to the parallel and orthogonal flow over the 1 m DEM. Even smaller earthflows, of approximately 3600 m², are
486 identified with the 5 m moving window MADstd. This advantage over previous, isotropic methods of calculating surface
487 roughness and identifying landslides indicates MADstd is an appropriate method for use in identifying and mapping
488 earthflows, though we caution that the DEM resolution size must be less than the scale of earthflow lineations.

489

490 Further, the decay of MADstd with age shows potential, particularly if it can be used as an absolute age when combined with
491 other dating methods. As time since earthflow activity increases, MADstd decreases in a strongly correlated (r -squared > 0.98)
492 linear relationship. Any error in the linear relationship remains similar despite the time frame considered. In contrast, other
493 surface roughness metrics like standard deviation of slope (SDS) have an exponential relationship with landslide age. When
494 calibrated to absolute dating, exponential relationships can result in errors are up to ± 1 ky for landslides that are 10 ky old
495 (LaHusen et al., 2016). Although we were unable to convert the MADstd relationship to an absolute age relationship for the
496 Teanaway, the MADstd roughness metric has potential as a more precise method to date older mass movements (~10 ky or
497 greater).

498 **6 Conclusion**

499 To examine controls on earthflow activity and resulting topographic disturbance in the Teanaway basin, we mapped and dated
500 earthflows using 1 m lidar and a new relative dating method that relies on flow directional surface roughness. The MADstd
501 metric appears well-suited to identifying and relatively dating earthflows, as it picks up linear roughness elements such as
502 lateral shear zones and levees, and is able to ignore the influence of dense vegetation on the elevation model. This is particularly
503 useful for densely vegetated areas, where other roughness metrics have difficulty and where object tracking is problematic to
504 apply. In addition to MADstd relative ages, we used radiocarbon and sedimentation ages to provide a few constraining absolute
505 ages; these ages indicate that 25% of earthflows in the Teanaway basin were active in the last few hundred years. Nearly all
506 (94%) of earthflows occur in the Teanaway and lower Roslyn formations, which contain interbedded basalt and rhyolite flows
507 along with paleosols and coarse sandstone. Slide aspect and slope roughly follow the orientation of the paleosol and volcanic
508 flow dip angles, suggesting a strong lithologic control on earthflow location and orientation. Most tributaries in the Teanaway
509 initiate on earthflow complexes, and experience valley width changes due to earthflow damming and associated upstream
510 widening. Despite some variability in source lithology, the selective transport of regolith and weathered material by earthflows
511 results in delivery of fine sediments. While this fine sediment poses a potential hazard for instream habitat, stream power is
512 sufficient to transport it downstream; therefore, the largest habitat disturbance provided by the earthflows is heterogeneity in
513 valley width.

514 **Data and code availability**

515 The diffusion simulation code and input files can be access on https://github.com/schanzs/JungleCk_diffusion. Landslide
516 information and dates are available at: <https://doi.org/10.5281/zenodo.5885660>

517 **Author contribution**

518 SAS conceptualized the study, SAS and APC contributed equally to study design and methodology. APC and SAS acquired
519 funding for the study. SAS wrote the paper with contributions from APC.

520 **Competing interests**

521 The authors declare that they have no conflict of interest.

522 **Acknowledgements**

523 Funding to APC was provided by the Patricia J. Buster grant from the Colorado College Geology Department and radiocarbon
524 sample analysis was paid for by Colorado College. We thank Matt Cooney for GIS help, and Jamie and Catharine Colee for
525 help in the field. Field work was conducted on the traditional territory of the Yakama and Wenatchi People. Suggestions from
526 three anonymous reviewers greatly improved the manuscript.

527 **References**

- 528 Abbe, T. B. and Montgomery, D. R.: Large woody debris jams, channel hydraulics and habitat formation in large rivers, 12,
529 201–221, 1996.
- 530 Agee, J. K.: Fire and weather disturbances in terrestrial ecosystems of the eastern Cascades, US. Department of Agriculture,
531 Pacific Northwest Research Station, 1994.
- 532 Agee, J. K.: Fire Ecology of Pacific Northwest Forests, Island Press, 513 pp., 1996.
- 533 Baum, R., Savage, W., and Wasowski, J.: Mechanics of earth flows, Proc. Int. Conf. FLOWS Sorrento Italy, 2003.
- 534 Beeson, H. W., Flitcroft, R. L., Fonstad, M. A., and Roering, J. J.: Deep-Seated Landslides Drive Variability in Valley Width
535 and Increase Connectivity of Salmon Habitat in the Oregon Coast Range, JAWRA J. Am. Water Resour. Assoc., 54, 1325–
536 1340, <https://doi.org/10.1111/1752-1688.12693>, 2018.
- 537 Bennett, G. L., Roering, J. J., Mackey, B. H., Handwerger, A. L., Schmidt, D. A., and Guillod, B. P.: Historic drought puts the
538 brakes on earthflows in Northern California, 43, 5725–5731, <https://doi.org/10.1002/2016GL068378>, 2016.
- 539 Berti, M., Corsini, A., and Daehne, A.: Comparative analysis of surface roughness algorithms for the identification of active
540 landslides, Geomorphology, 182, 1–18, <https://doi.org/10.1016/j.geomorph.2012.10.022>, 2013.
- 541 Booth, A. M., LaHusen, S. R., Duvall, A. R., and Montgomery, D. R.: Holocene history of deep-seated landsliding in the North
542 Fork Stillaguamish River valley from surface roughness analysis, radiocarbon dating, and numerical landscape evolution
543 modeling, 122, 456–472, <https://doi.org/10.1002/2016JF003934>, 2017.
- 544 Braun, J. and Willett, S. D.: A very efficient O(n), implicit and parallel method to solve the stream power equation governing
545 fluvial incision and landscape evolution, Geomorphology, 180–181, 170–179,
546 <https://doi.org/10.1016/j.geomorph.2012.10.008>, 2013.
- 547 Burnett, K. M., Reeves, G. H., Miller, D. J., Clarke, S., Vance-Borland, K., and Christiansen, K.: Distribution of Salmon-
548 Habitat Potential Relative to Landscape Characteristics and Implications for Conservation, Ecol. Appl., 17, 66–80,
549 [https://doi.org/10.1890/1051-0761\(2007\)017\[0066:DOSPRT\]2.0.CO;2](https://doi.org/10.1890/1051-0761(2007)017[0066:DOSPRT]2.0.CO;2), 2007.
- 550 Cerovski-Darriau, C. and Roering, J. J.: Influence of anthropogenic land-use change on hillslope erosion in the Waipaoa River
551 Basin, New Zealand, 41, 2167–2176, <https://doi.org/10.1002/esp.3969>, 2016.
- 552 Cle Elum Tribune: Cle Elum Tribune, March 20, 1891 issue, , 20th March, page 4, 1891.

553 Clubb, F. J., Weir, E. F., and Mudd, S. M.: Continuous measurements of valley floor width in mountainous landscapes, *Earth*
554 *Surf. Dynam. Discuss.* [preprint], <https://doi.org/10.5194/esurf-2022-2>, in review, 2022.

555 Coe, J. A.: Regional moisture balance control of landslide motion: Implications for landslide forecasting in a changing climate,
556 *Geology*, 40, 323–326, <https://doi.org/10.1130/G32897.1>, 2012.

557 Fratkin, M. M., Segura, C., and Bywater-Reyes, S.: The influence of lithology on channel geometry and bed sediment
558 organization in mountainous hillslope-coupled streams, 45, 2365–2379, <https://doi.org/10.1002/esp.4885>, 2020.

559 Goetz, J. N., Bell, R., and Brenning, A.: Could surface roughness be a poor proxy for landslide age? Results from the Swabian
560 Alb, Germany, 39, 1697–1704, <https://doi.org/10.1002/esp.3630>, 2014.

561 Graumlich, L. J. and Brubaker, L. B.: Reconstruction of annual temperature (1590–1979) for Longmire, Washington, derived
562 from tree rings, 25, 223–234, 1986.

563 Guerriero, L., Bertello, L., Cardozo, N., Berti, M., Grelle, G., and Revellino, P.: Unsteady sediment discharge in earth flows:
564 A case study from the Mount Pizzuto earth flow, southern Italy, *Geomorphology*, 295, 260–284,
565 <https://doi.org/10.1016/j.geomorph.2017.07.011>, 2017.

566 Handwerker, A. L., Roering, J. J., and Schmidt, D. A.: Controls on the seasonal deformation of slow-moving landslides, *Earth*
567 *Planet. Sci. Lett.*, 377–378, 239–247, <https://doi.org/10.1016/j.epsl.2013.06.047>, 2013.

568 Hungr, O., Leroueil, S., and Picarelli, L.: The Varnes classification of landslide types, an update, *Landslides*, 11, 167–194,
569 <https://doi.org/10.1007/s10346-013-0436-y>, 2014.

570 Johnstone, S. A. and Hilley, G. E.: Lithologic control on the form of soil-mantled hillslopes, *Geology*, 43, 83–86,
571 <https://doi.org/10.1130/G36052.1>, 2015.

572 Kittitas County Centennial Committee: A history of Kittitas County, Washington, Taylor Publishing Company, Dallas, TX,
573 693 pp., 1989.

574 LaHusen, S. R., Duvall, A. R., Booth, A. M., and Montgomery, D. R.: Surface roughness dating of long-runout landslides near
575 Oso, Washington (USA), reveals persistent postglacial hillslope instability, *Geology*, 44, 111–114,
576 <https://doi.org/10.1130/G37267.1>, 2016.

577 Mackey, B. H. and Roering, J. J.: Sediment yield, spatial characteristics, and the long-term evolution of active earthflows
578 determined from airborne LiDAR and historical aerial photographs, Eel River, California, *GSA Bull.*, 123, 1560–1576,
579 <https://doi.org/10.1130/B30306.1>, 2011.

580 Malet, J.-P., Laigle, D., Remaître, A., and Maquaire, O.: Triggering conditions and mobility of debris flows associated to
581 complex earthflows, *Geomorphology*, 66, 215–235, <https://doi.org/10.1016/j.geomorph.2004.09.014>, 2005.

582 Marshall, J. A., Roering, J. J., Bartlein, P. J., Gavin, D. G., Granger, D. E., Rempel, A. W., Praskievicz, S. J., and Hales, T.
583 C.: Frost for the trees: Did climate increase erosion in unglaciated landscapes during the late Pleistocene?, *Sci. Adv.*, 1,
584 e1500715, <https://doi.org/10.1126/sciadv.1500715>, 2015.

585 Martin, Y.: Modelling hillslope evolution: linear and nonlinear transport relations, *Geomorphology*, 34, 1–21,
586 [https://doi.org/10.1016/S0169-555X\(99\)00127-0](https://doi.org/10.1016/S0169-555X(99)00127-0), 2000.

587 May, C., Roering, J., Eaton, L. S., and Burnett, K. M.: Controls on valley width in mountainous landscapes: The role of
588 landsliding and implications for salmonid habitat, *Geology*, 41, 503–506, <https://doi.org/10.1130/G33979.1>, 2013.

589 McKean, J. and Roering, J.: Objective landslide detection and surface morphology mapping using high-resolution airborne
590 laser altimetry, *Geomorphology*, 57, 331–351, [https://doi.org/10.1016/S0169-555X\(03\)00164-8](https://doi.org/10.1016/S0169-555X(03)00164-8), 2004.

591 McSaveney, M. J. and Griffiths, G. A.: Drought, rain, and movement of a recurrent earthflow complex in New Zealand,
592 *Geology*, 15, 643–646, [https://doi.org/10.1130/0091-7613\(1987\)15<643:DRAMOA>2.0.CO;2](https://doi.org/10.1130/0091-7613(1987)15<643:DRAMOA>2.0.CO;2), 1987.

593 Montgomery, D. R. and Buffington, J. M.: Channel-reach morphology in mountain drainage basins, *Geol. Soc. Am. Bull.*,
594 109, 596–611, 1997.

595 Moon, S., Page Chamberlain, C., Blisniuk, K., Levine, N., Rood, D. H., and Hilley, G. E.: Climatic control of denudation in
596 the deglaciated landscape of the Washington Cascades, *Nat. Geosci.*, 4, 469–473, <https://doi.org/10.1038/ngeo1159>, 2011.

597 Nereson, A. L. and Finnegan, N. J.: Drivers of earthflow motion revealed by an 80 yr record of displacement from Oak Ridge
598 earthflow, Diablo Range, California, USA, *GSA Bull.*, 131, 389–402, <https://doi.org/10.1130/B32020.1>, 2018.

599 NFTWA: North Fork Teanaway Watershed Analysis: Resource Assessment Report. Prepared by: Boise Cascade Corporation;
600 Cascade Environmental Services, Inc.; Mary Raines, Geomorphologist; Shannon & Wilson, Inc.; Karen F. Welch, Hydrologist;
601 Forster Wheeler; Caldwell & Associates; Ecologic, Inc.; Yakama Indian Nation; EDAW, Inc., Boise, ID., 1996.

602 Porter, S. C.: Pleistocene glaciation in the southern part of the North Cascade Range, Washington, *Geol. Soc. Am. Bull.*, 87,
603 61–75, [https://doi.org/10.1130/0016-7606\(1976\)87<61:PGITSP>2.0.CO;2](https://doi.org/10.1130/0016-7606(1976)87<61:PGITSP>2.0.CO;2), 1976.

604 Quantum Spatial: Teanaway streams topobathymetric LiDAR, 2015.

605 Quantum Spatial: Yakima Wildfire Lidar Survey, Available at: <https://lidarportal.dnr.wa.gov/>. Accessed on May 24, 2021,
606 2018.

607 Reimer, P. J., Austin, W. E. N., Bard, E., Bayliss, A., Blackwell, P. G., Ramsey, C. B., Butzin, M., Cheng, H., Edwards, R. L.,
608 Friedrich, M., Grootes, P. M., Guilderson, T. P., Hajdas, I., Heaton, T. J., Hogg, A. G., Hughen, K. A., Kromer, B., Manning,
609 S. W., Muscheler, R., Palmer, J. G., Pearson, C., Plicht, J. van der, Reimer, R. W., Richards, D. A., Scott, E. M., Southon, J.
610 R., Turney, C. S. M., Wacker, L., Adolphi, F., Büntgen, U., Capano, M., Fahrni, S. M., Fogtmann-Schulz, A., Friedrich, R.,
611 Köhler, P., Kudsk, S., Miyake, F., Olsen, J., Reinig, F., Sakamoto, M., Sookdeo, A., and Talamo, S.: The IntCal20 Northern
612 Hemisphere Radiocarbon Age Calibration Curve (0–55 cal kBP), *Radiocarbon*, 62, 725–757,
613 <https://doi.org/10.1017/RDC.2020.41>, 2020.

614 Reiners, P. W., Ehlers, T. A., Mitchell, S. G., and Montgomery, D. R.: Coupled spatial variations in precipitation and long-
615 term erosion rates across the Washington Cascades, *Nature*, 426, 645–647, <https://doi.org/10.1038/nature02111>, 2003.

616 Schanz, S. A. and Montgomery, D. R.: Lithologic controls on valley width and strath terrace formation, *Geomorphology*, 258,
617 58–68, <https://doi.org/10.1016/j.geomorph.2016.01.015>, 2016.

618 Schanz, S. A., Montgomery, D. R., and Collins, B. D.: Anthropogenic strath terrace formation caused by reduced sediment
619 retention, *Proc. Natl. Acad. Sci.*, 116, 8734–8739, <https://doi.org/10.1073/pnas.1814627116>, 2019.

620 Struble, W. T., Roering, J. J., Black, B. A., Burns, W. J., Calhoun, N., and Wetherell, L.: Dendrochronological dating of
621 landslides in western Oregon: Searching for signals of the Cascadia A.D. 1700 earthquake, *GSA Bull.*, 132, 1775–1791,
622 <https://doi.org/10.1130/B35269.1>, 2020.

623 Sweeney, K. E., Roering, J. J., and Ellis, C.: Experimental evidence for hillslope control of landscape scale,
624 <https://doi.org/10.1126/science.aab0017>, 2015.

625 Tabor, R. W., Waitt, Jr., R. B., Frizzell, Jr., V. A., Swanson, D. A., Byerly, G. R., and Bentley, R. D.: Geologic map of the
626 Wenatchee 1:100,000 quadrangle, central Washington, U.S. Geological Survey, Menlo Park, CA, 1982.

627 Tabor, R. W., Frizzell, V. A., JR., Vance, J. A., and Naeser, C. W.: Ages and stratigraphy of lower and middle Tertiary
628 sedimentary and volcanic rocks of the central Cascades, Washington: Application to the tectonic history of the Straight Creek
629 fault, *GSA Bull.*, 95, 26–44, [https://doi.org/10.1130/0016-7606\(1984\)95<26:AASOLA>2.0.CO;2](https://doi.org/10.1130/0016-7606(1984)95<26:AASOLA>2.0.CO;2), 1984.

630 Trevisani, S. and Cavalli, M.: Topography-based flow-directional roughness: potential and challenges, *Earth Surf. Dyn.*, 4,
631 343–358, <https://doi.org/10.5194/esurf-4-343-2016>, 2016.

632 Trevisani, S. and Rocca, M.: MAD: robust image texture analysis for applications in high resolution geomorphometry, *Comput.*
633 *Geosci.*, 81, 78–92, <https://doi.org/10.1016/j.cageo.2015.04.003>, 2015.

634 U.S. Geological Survey: The StreamStats program for Washington: <http://water.usgs.gov/osw/streamstats/Washington.html>,
635 last access: 5 January 2018, 2012.

636 Waples, R. S., Pess, G. R., and Beechie, T.: Evolutionary history of Pacific salmon in dynamic environments, *Evol. Appl.*, 1,
637 189–206, <https://doi.org/10.1111/j.1752-4571.2008.00023.x>, 2008.

638 Wright, C. S. and Agee, J. K.: Fire and Vegetation History in the Eastern Cascade Mountains, Washington, *Ecol. Appl.*, 14,
639 443–459, <https://doi.org/10.1890/02-5349>, 2004.